High Performance and Stackable Trampoline Like-Triboelectric Vibration Energy Harvester for In-Situ Powering Sensor Node with Data Wirelessly Transmitted Over 1000-m

Hongyong Yu, Ziyue Xi, Hengxu Du, Hengyi Yang, Zian Qian, Xinyang Guo, Yuanye Guo, Yue Huang, Taili Du,* and Minyi Xu*

Addressing the power supply challenges of wireless sensor nodes is pivotal for advancing the development of the Internet of Things (IoT). This work proposes a high performance and stackable trampoline like-triboelectric vibration energy harvester (T-TVEH) that can efficiently harvest ultra-wideband vibrational energy for in-situ powering of sensor nodes. The unique structural design and material selection enables T-TVEH to represent a breakthrough in terms of both working bandwidth and power density compared to recent research efforts of vibration energy harvesting. Specifically, the working bandwidth and the peak power density of T-TVEH is 192 Hz and 5.9 W m^{-2}, which are higher than previous related studies by 156% and 59.2%, respectively. Based on the excellent performance of the T-TVEH, a wireless sensor node for monitoring machinery condition is constructed. Temperature, humidity, and frequency information are successfully acquired and transmitted to 1000-m through the wireless sensor node, which is nine times improved compared to related studies. Meanwhile, it achieves fully self-powered wireless operation monitoring and abnormal alarm on a real ship's marine diesel engine. Overall, this study proposed an innovative solution for in-situ power supply of wireless sensor nodes, which has broad application prospects in the field of the IOT.

1. Introduction

The Internet of Things (IoT) connects various physical devices,[1] sensors,[2] software,[3] and other technologies to realize the collection, exchange, and remote control of information, which provides more possibilities for people's lives, work, and industries.[4–6] To achieve seamless connection and efficient operation of the IoT,[7] a large number of wireless sensor networks (WSNs) are essential.[8] Therefore, the WSNs are widely distributed in every corner to provide environmental conditions, device status and other important data for the IoT.[9–11] However, the utilization of wired power supply methods constrains the flexibility, widespread deployment, and practical application of sensors.[12] Furthermore, the traditional battery power supply mode faces the challenges of limited lifespan, high maintenance costs, and the difficulty of replacing batteries in harsh environments.[13–16] In response to the aforementioned challenges, harnessing ambient energy achieve in-situ power provisioning of WSNs represents a highly innovative and rational approach.[17] Abundant and wasted vibration energy exists in factories, bridges, transportation equipment, and other places, which can be converted into electricity to power the WSNs.[18] The randomness and diversity of vibration sources present challenges in harvesting energy through different methods.[19–21] Therefore, it is crucial to further explore suitable vibration energy harvesters (VEH) to enable in-situ energy supply for WSNs.[22]

To address the aforementioned issues, Wang proposed the triboelectric nanogenerator (TENG) based on the combination of triboelectrification and electrostatic induction.[23–25] This proposal has garnered significant interest from researchers due to its excellent performance, wide range of material availability, strong adaptability, ease of manufacturing, low cost and so on.[26–28] The TENG exhibits the potential to harvest vibration energy in a wide bandwidth owing to its unique working mechanism.[29] Numerous scholars have conducted extensive research on VEHs based on TENG (V-TENG),[30–33] furthering the advancement of the IoT. However, several challenges still need resolution, significantly hindering the practical application of VEHs. On the

H. Yu, Z. Xi, H. Du, H. Yang, Z. Qian, X. Guo, Y. Guo, Y. Huang, T. Du, M. Xu
Dalian Key Lab of Marine Micro/Nano Energy and Self-powered Systems
Marine Engineering College
Dalian Maritime University
Dalian 116026, China
E-mail: dutaili@dlmu.edu.cn; xuminyi@dlmu.edu.cn
T. Du
Collaborative Innovation Research Institute of Autonomous Ship
Dalian Maritime Transportation Engineering College
Dalian Maritime University
Dalian 116026, China

**ADVANCED
SCIENCE NEWS**

www.advancedsciencenews.com

**ADVANCED
ENERGY
MATERIALS**

www.advenergymat.de

one hand, the WSNs are commonly employ multiple sensors with different functions to acquisition and wireless transmission comprehensive information, which leads to the high power consumption during the operation of the WSNs. To achieve fully self-powering for the WSNs, researchers have made many efforts to boost the performance of V-TENG. Wu et al. proposed a spring-mass-based TENG utilizing an inner spring and an outer helix structure to increase the contact area and thus improve the output performance.[10] Qi et al. proposed a two stoppers TENG constituting a dual-output charge pump that increases the surface charge density by about 14 times.[34] While these efforts provide innovative ways to increase the power output of the TENG, more effective methods still necessary to be explored for further improvements thereby meeting the requirement of power supply for the WSNs. On the other hand, the VEHs are usually designed as spring-assisted resonant structures to enhance the vibration effect for high performance output.[35–37] Although they demonstrate excellent performance in a limited bandwidth around the resonant frequency, their output deteriorates beyond this range, rendering harvesters inefficient in practical applications.[38] Therefore, it is essential to explore methods to increase the effective working frequency bandwidth of VEHs. To broaden the bandwidth, nonlinear structures are widely utilized to design VEHs.[32,39,40] Zhang et al. proposed a kirigami-inspired TENG, which can harvest broadband vibration energy from 2 to 49 Hz.[41] Cheng et al. proposes a novel multi-mode TENG broaden the frequency response range by designing an S-beam that can reduce high-order modal frequencies.[42] The working frequency band of V-TENG has been improved through the efforts of scholars. However, the performance of these V-TENGs is mainly dependent on the amplitude amplification capability of the structure, which limits further improvement of the bandwidth and favorable performance in high frequency and low-amplitude vibration conditions. Therefore, it continues challenging to broaden the frequency band and enhance the output performance of V-TENG.

In this work, a high performance and stackable trampoline like-triboelectric vibration energy harvester (T-TVEH) is proposed for efficiently harvest vibrational energy in broadband frequency range. The T-TVEH consists of a base plate with evenly distributed holes, additional mass, a conductive sponge, a conductive fabric, a FEP film with conductive ink printed on one side adhered to an iron plate, and silicone. The additional mass enhances the amplitude of the FEP film and the force in contact with the conductive fabric. The base plate with holes improves electrical output performance and working bandwidth of T-TVEH. The unique structural design and selection of materials enables T-TVEH to generate excellent electrical output performance over an ultra-wideband rather than being limited to the vibration conditions that low frequency and large amplitude. The experimental results indicate that its capability to harvest energy in an ultra-wide band of 8–200 Hz, surpassing previous studies by 156%. The T-TVEH's excellent durability is demonstrated through durability testing and SEM image analysis. Simultaneously, it achieves a power density of 5.9 W m^{-2}, enabling the charging of a 0.1 F supercapacitor from 0 to 3.5 V in 1154 s. Furthermore, a fully self-powered wireless sensor node for monitoring machinery condition is constructed based on the excellent performance of T-TVEH.

The wireless sensor node can collect equipment operation information, provides terminal display, and abnormal alarm by wireless communication from a distance of 1000-m. Meanwhile, it achieves fully self-powered wireless operation monitoring and abnormal alarm on a marine diesel engine of real ship. The remarkable performance enables the T-TVEH to have great potential in vibration energy harvesting and machinery monitoring.

2. Results and Discussion

2.1. Application and Structure of the T-TVEH

Figure 1a illustrates the application scenario of the T-TVEH, which converts mechanical vibration energy into electrical energy to provide in-situ power for the wireless sensor node for monitoring machinery condition. The T-TVEH consists of a base plate with evenly distributed holes, additional mass, a conductive sponge, a conductive fabric, a FEP film with conductive ink printed on one side adhered to an iron plate, and silicone. The silicone is designed with a distinctive four-corner structure to ensure stability during vibrations and reduced device size. The additional mass increases the mass inertia of the FEP film and contact force, thereby enhancing the performance of the T-TVEH. The hole structure of the base plate mitigates the influence of differential pressure on the movement of the FEP film, ensuring excellent contact effect during the contact-separation process of the two friction layers. In this work, wireless sensors are determined and utilized for the collection of critical parameters, including the vibration frequency of equipment, surrounding temperature, and humidity, which are of great significance in assessing the working condition of the equipment. Compared with Bluetooth, Wifi, etc., the Lora-based wireless communication module has the advantages of long-distance transmission and low power consumption, so it is used for wireless transmission of information. Finally, the information that represents the operating status of mechanical equipment is displayed on computers and OLED screens, with different colored LEDs indicating abnormal states.

Due to the distinctive structural design of the T-TVEH, it can efficiently harvest vibration energy in an ultra-broad frequency range. The T-TVEH represents a breakthrough in terms of both working bandwidth and power density compared to recent research efforts in the field of vibration energy harvesting (Table S1 Supporting Information).[10,18,29,31,32,39,41,43–46] Specifically, the T-TVEH can harvest vibration energy across an ultra-wide bandwidth of 8–200 Hz, which is an improvement of 156% compared to recent related research work (Figure 1b). As illustrated in Figure 1c, the T-TVEH achieves a peak power of up to 5.9 W m^{-2}, which is a 59.2% increase compared to the best results from recent related research work. In addition, a LoRa-based wireless monitoring system, characterized by low power consumption and long-distance signal transmission, has been successfully constructed. The temperature, humidity, and vibration frequency information are successfully captured and transmitted up to 1000-m, which is the farthest transmission distance to the best of our knowledge among previously reported WSNs powered by TENG (Figure 1d and Table S2, Supporting Information).[37,47–53]
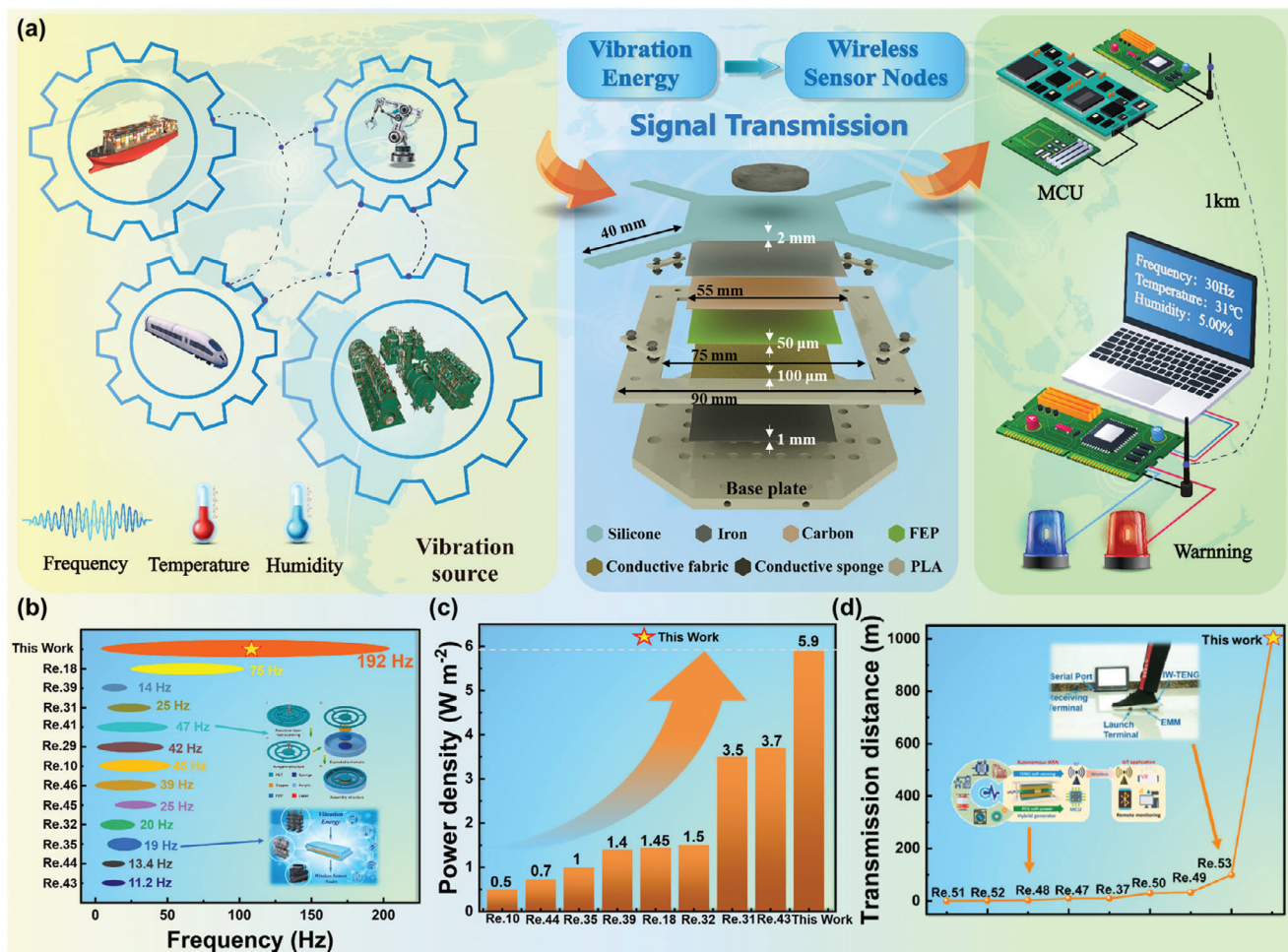
Figure 1. Application scenarios of the T-TVEH. a) Application scenarios and structure schematic of the T-TVEH. Comparison of b) the working frequency band range, c) the power density, and d) the transmission distance with the recent research.

2.2. Kinematic Characteristics and Working Principle of the T-TVEH

As shown in **Figure 2a**, to investigate the electrical output performance (EOP) of the T-TVEH, optimize the structural design, and analyze the motion characteristics, the test platform is established. The shaker is employed to simulate mechanical vibration, with and frequency (f) controlled by a signal generator, and the amplitude (A) amplified by a power amplifier. The relative displacement between two dielectric materials is measured by a laser displacement sensor, while the maximum acceleration (a_m) of the shaker is quantified by an acceleration sensor. Additionally, a high-speed camera is employed to capture the dynamic response of the T-TVEH. Finally, the acquired signals are displayed and processed through a LabView-based computer. The charge transfer and the high-speed images of the two dielectric materials in different motion states are shown in Figure 2b. In the initial stage, two dielectric materials make contact with each other due to gravity of additional mass, as shown in Figure 2b(i). The surfaces of the FEP film and conductive fabric generate equal amounts of positive and negative charges during the contact period. Subsequently, the base plate ascends from lowest to highest

position under the vibration excitation. Throughout this process, the FEP film maintains continuous contact with the conductive fabric, thereby generating a large amount of charge transfer. As the base plate ascends to the highest point and then descends with the shaker, the FEP film maintains upward movement due to the mass inertia of the additional mass, leading it to separate from the conductive fabric (Figure 2b(ii)). This induces the flow of electrons from the ink electrode adhered to the FEP film to the conductive fabric, thereby equalizing the potential difference between two electrodes. Consequently, a current flowing from the conductive fabric to the FEP film is generated. The relative displacement of the two dielectric materials increases as the base plate lowers and the FEP film raises (Figure 2b(iii)). The charge transfer reaches maximum when the FEP film reaches the highest position. The FEP film drops rapidly from its highest position due to the gravity and the elasticity of the silicone, and stops falling when it collides with the conductive fabric (Figure 2b(iv)). At this stage, a current opposite to that in Figure 2b(ii) is generated during its descent to equalize the potential difference. Finally, the FEP film returns to its initial position, and the initial electrostatic balance is re-established. Thereby, an alternative current signal is achieved in this complete working process of the
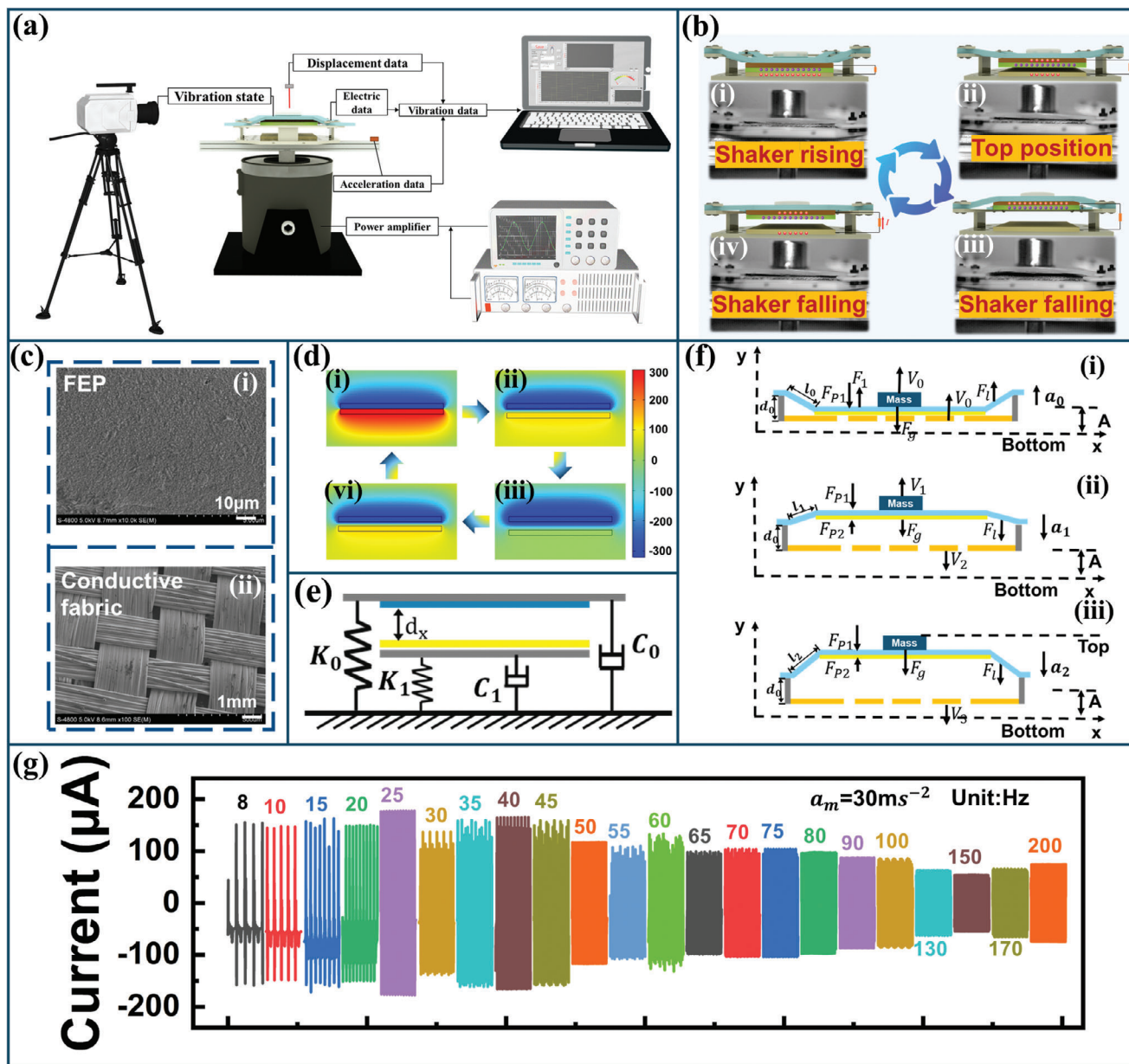
**ADVANCED
SCIENCE NEWS**

www.advancedsciencenews.com

**ADVANCED
ENERGY
MATERIALS**

www.advenergymat.de

Figure 2. Kinematic characteristics and working principle of the T-TVEH. a) Diagram of the test platform. b) The charge transfer process in different motion states. c) The SEM image of i) the FEP film and ii) the conductive fabric. d) Potential distribution of two dielectric materials under different states of motion. e) Theoretical model of the T-TVEH. f) Force analysis of the T-TVEH under different motion states. g) The I_{sc} of the T-TVEH at a_m = 30 m s^{-2}.

T-TVEH. According to the working modes of the TENG, the T-TVEH works based on the contact-separation mode. Therefore, the short-circuit current (I_{sc}), and transferred charge (Q_{sc}) are important parameters for evaluating the EOP of TENG, which are given by the following equations:[54]

$$Q_{SC} = \frac{S\sigma\gamma(t)}{\varepsilon_0} \tag{1}$$

$$I_{SC} = \frac{dQ_{sc}}{dt} = \frac{S\sigma d_c}{\left(d_c + \gamma(t)\right)^2}\frac{dx}{dt} = \frac{S\sigma d_c v(t)}{\left(d_c + \gamma(t)\right)^2} \tag{2}$$

here, S is the area of the dielectric material, σ is the charge density, $\gamma(t)$ is the distance between the two dielectric materials, ε_0 is the relative dielectric constant, and d_c is the thickness of dielectrics material. The above equation shows that the charge density of dielectric material, the contact separation distance, and the kinetic characteristic are the crucial in determining the EOP of TENG. Triboelectrification results from electron transfer between two atoms due to an overlapping electron cloud lowering the potential barrier.[55] Therefore, the ability of the two dielectric materials to gain and lose electrons, the effective contact area, and the magnitude of the contact force will all determine the

surface charge density. The FEP film has been selected as a dielectric material owing to its electret and easily obtainable electrons characteristics. Meanwhile, the surface of the FEP film is sanded by using 1000-grit sandpaper to increase the effective contact area. The corresponding scanning electron microscope (SEM) images of the sanded FEP film are displayed in Figure 2c(i). The conductive fabric has been selected as a dielectric material owing to their excellent permeability (Figure 2c(ii)) and easily lose electrons characteristics.[56] As shown in Figure 2d, the potential distribution of two dielectric materials subjected to contact-detachment motion is further simulated by using COMSOL software.

To analyze the kinematic characteristics of the T-TVEH, as shown in Figure 2e, the T-TVEH is modeled as a single-degree-of-freedom system with nonlinear characteristics. In this dynamic system, the silicone and sponge are respectively equivalent to springs with different elastic coefficients. Since the introduction of the pedestal adds a nonlinear force ($F_{\_nonlinear}$) to the mass-spring-damped system, the differential equation of motion is given as follows:

$$m * \gamma''(t) + C_1 * \gamma'(t) + k_1 * \gamma(t) = F(t) \tag{3}$$

$$m * \gamma''(t) + (C_0 + C_1) * \gamma'(t) + (K_0 + K_1) * \gamma(t) = F(t) + F\_nonlinear \tag{4}$$

where, m is the total weight of the FEP film with additional mass, C_0 and C_1 are the damping at different positions, K_0 and K_1 are the equivalent elasticity coefficients of conductive sponge and silicone, respectively, and $F(t)$ is the thrust force exerted by the shaker on the T-TVEH. The dynamics of the T-TVEH can be described by Equation (3) when the FEP film is separated from the conductive fabric and further described by Equation (4) when the FEP film is in contact with the conductive fabric. Equation (3) was solved using the commercial software Matlab to obtain the displacement response of the T-TVEH, as shown in Figure S1 (Supporting Information). It can be seen that the displacement gradually increases as the mass and acceleration increase. As shown in Figure 2f, the effects of the structural parameters on the kinetic characteristics of the T-TVEH are investigated from the perspective of energy conversion. As shown in Figure 2f(i), the T-TVEH and the shaker move upward together with the a_0 of acceleration. During this process, the FEP film is subjected to a downward gravitational force F_g generated by the additional mass and silicone, an upward elastic force F_l exerted by the silicone, a thrust force F_t exerted by the shaker, and a downward air resistance force F_p. The total energy E obtained by the FEP film with additional mass can be expressed as:

$$E = \int_0^A m \cdot a(\gamma)\,d\gamma = \frac{1}{2} m \cdot a_m \cdot A \tag{5}$$

The FEP film then moves rapidly downward with the shaker, while it continues to move upward due to mass inertia. At this time, the energy E gained by the FEP film is converted into kinetic energy (E_k), gravitational potential energy (E_g), energy consumed by air resistance (E_d) and the elastic potential energy of the silicone (E_l). The gravitational potential energy can be expressed as:

$E_g = mg\Delta\gamma_1$, where $\Delta\gamma_1$ is the displacement of FEP film moving upward. The E_l can be expressed as:

$$E_l = \int_{\Delta l}^0 -k\gamma\,d\gamma = \frac{1}{2} k \left(\sqrt{(\Delta\gamma_1 + \Delta\gamma_2)^2 + \frac{(L_2 - L_1)^2}{4}} - l_1 \right)^2 \tag{6}$$

Here, k represents the silicone equivalent coefficient of elasticity, L_1 and L_2 represent the length of the FEP film and base plate, respectively. $\Delta\gamma_2$ is the drop displacement of the base plate, which can be expressed as: $\Delta\gamma_2 = \frac{a_0^3}{2a_1^2 f^2}$. The energy required to overcome air resistance $E_d = \int \frac{1}{2} C_d \rho s v^2\,d\gamma$, where C_d is the resistance coefficient, which is influenced by the permeability of the base plate, ρ is air density. According to conservation of energy, when the FEP film reaches its highest position, All the total energy E is converted into potential energy. Thus, there is the following equation:

$$m a_m A = mg\Delta\gamma_1 + \frac{1}{2}k \left(\sqrt{(\Delta\gamma_1 + \Delta\gamma_2)^2 + \frac{(L_2 - L_1)^2}{4}} - l_1 \right)^2$$

$$+ \int \frac{1}{2} C_d \rho s v^2\,d\gamma \tag{7}$$

As a result, the relative displacement of the T-TVEH is influenced by external vibration, additional mass, elongation of silicone, and permeability of the base plate, all of which will be optimized in further experiments.

As shown in Figure 2g, the I_{sc} and Q_{sc} of the T-TVEH in the vibration frequency is 8–200 Hz and acceleration constant at 30 m s^{-2}. It can be seen that the maximum values of I_{sc} and Q_{sc} are 178.5 µA and 485.5 nC, respectively, and it still has excellent electrical output performance (I_{sc} = 75.2 µA, Q_{sc} = 232.2 nC) even at the frequency rises to 200 Hz. This indicates that, owing to its unique structural design and increased inertial forces, the FEP film can undergo contact- separation motion with the conductive fabric as long as a vibration source exists. This enables the T-TVEH to harvest energy at low amplitudes and an ultra-wide bandwidth range of vibration excitation.

2.3. Effect of Additional Mass on Output Performance of the T-TVEH

According to the above analysis, the additional mass has a critical impact on the kinematic characteristics of the T-TVEH, which will also play a key role on the EOP of it. To explore the impact of additional mass on the EOP in the frequency from 8 to 250 Hz, the I_{sc} and Q_{sc} of the T-TVEH are tested with the additional mass of 0, 20, 40, 60, 80 g, respectively (**Figure 3a**; Figure S2, Supporting Information). Test results show that the additional mass greatly improves the EOP and the bandwidth of the T-TVEH. The EOP of the T-TVEH without additional mass exhibits a general trend of increasing and then decreasing with frequency, peaking at 25 Hz (I_{sc} = 103 µA, Q_{sc} = 259 nC) and then decreasing rapidly (e.g., the current is only 2 µA at 40 Hz). When an additional mass of 20 g is applied, the I_{sc} of the T-TVEH reaches a maximum of 154.1 µA at 15 Hz, which is 1.6 times that of without
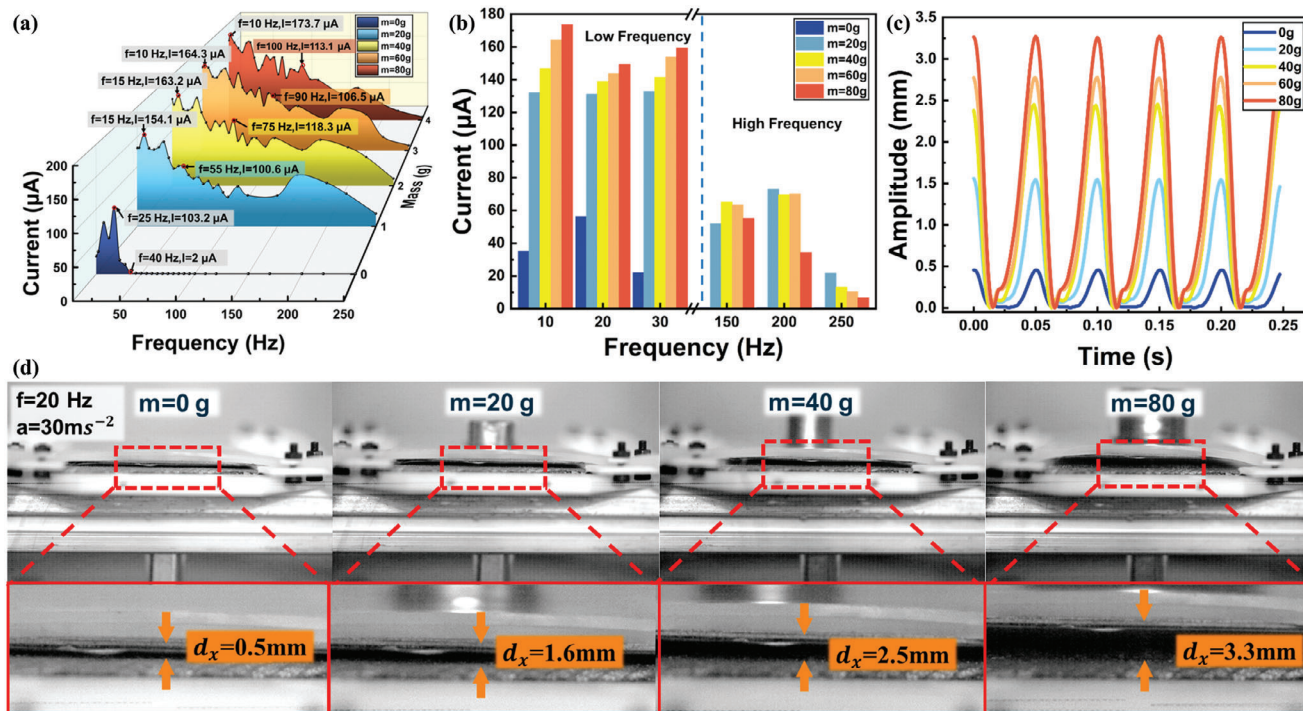
**ADVANCED
SCIENCE NEWS**

www.advancedsciencenews.com

**ADVANCED
ENERGY
MATERIALS**

www.advenergymat.de

Figure 3. Effect of additional mass on T-TVEH. a) Comparison of the I_{sc} of T-TVEH with different additional mass at the frequency range of 8–250 Hz. b) Comparison of the I_{sc} of the T-TVEH with different additional mass at low frequency and high frequency range. c) Comparison of relative displacements of the FEP film with different additional masses. d) The maximum relative displacement between two dielectric materials was recorded by a high-speed camera.

additional mass. According to Equation (5), the additional mass can increase the energy E obtained by the FEP film from the vibration excitation, which will increase $\Delta\gamma_1$ during separation and the force upon contact to enhance the EOP of T-TVEH. To evaluate the bandwidth of T-TVEH, Δf is defined as: $\Delta f = f_1 - f_0$, where f_0 is 8 Hz, and f_1 is the frequency that the I_{sc} of T-TVEH will be less than 100 μA. Obviously, the f_1 is 55 Hz ($I_{sc} = 103.2$ μA) with the additional mass of 20 g, which increases to 100 Hz ($I_{sc} = 113.1$ μA) at the additional mass increases to 80 g. With additional mass increases, Δf gradually improves from 32 to 92 Hz. This clearly shows the enhancement of the T-TVEH bandwidth with additional mass. In addition, the effect of additional mass on the EOP varies in different frequency band ranges. Figure 3b analyzes the I_{sc} of the T-TVEH with different additional masses at the low and high frequency ranges, respectively. The results demonstrate that the EOP of the T-TVEH gradually enhances with increasing weight in the low frequency range. However, the EOP of the T-TVEH increases gradually with increasing mass and then decreases, indicating an optimal mass at the high frequency range. The optimal mass decreases along with increasing frequency. As shown in the Figure S3 (Supporting Information), to further explore the EOP of T-TVEH when the mass exceeds 80g, the I_{sc} of the T-TVEH with additional mass form 0 to 100 g is evaluated at the frequency of 30 Hz. The experimental results show that the current of the T-TVEH increases dramatically when the additional mass is increased from 0 to 60 g. However, the I_{sc} of the T-TVEH is relatively stable when the additional mass is increased from 60 to 100 g. This is due to the charge transfer reaching saturation and unable to further increase.

To investigate the effect of additional mass on the kinematic state of the T-TVEH, a laser displacement sensor is used to measure the maximum relative displacement of the FEP film with different additional masses under the same excitation conditions. Figure 3c shows that the relative displacement of the FEP film, inhibited by silicone elasticity and air resistance is only 0.5 mm when no mass is attached. The relative displacement gradually increases with additional mass, reaching 3.5 mm with an additional mass of 80 g. Figure 3d and Movie S1 (Supporting Information) employ a high-speed camera to record the movement process of the T-TVEH with various additional masses under the same vibrational excitation. Clearly, the effect of additional mass on the motion of the T-TVEH is consistent with the above conclusion. In short, these results demonstrate the additional mass increases the relative displacement during separation and the force upon contact, thereby enhancing the EOP and the bandwidth of T-TVEH.

2.4. Effect of the Main Structural Parameters on EOP of the T-TVEH

In addition to additional mass, the main structural parameters of the T-TVEH, as shown in **Figure 4a**, also influence the kinematic characteristics and the EOP of the T-TVEH. These critical parameters discussed in this work encompass silicone elongation, spacer size, and different base plate types. Among them, the silicone elongation is expressed as $L_e = l_0/l$, and three different types of base plates, distinguished by varying degrees of
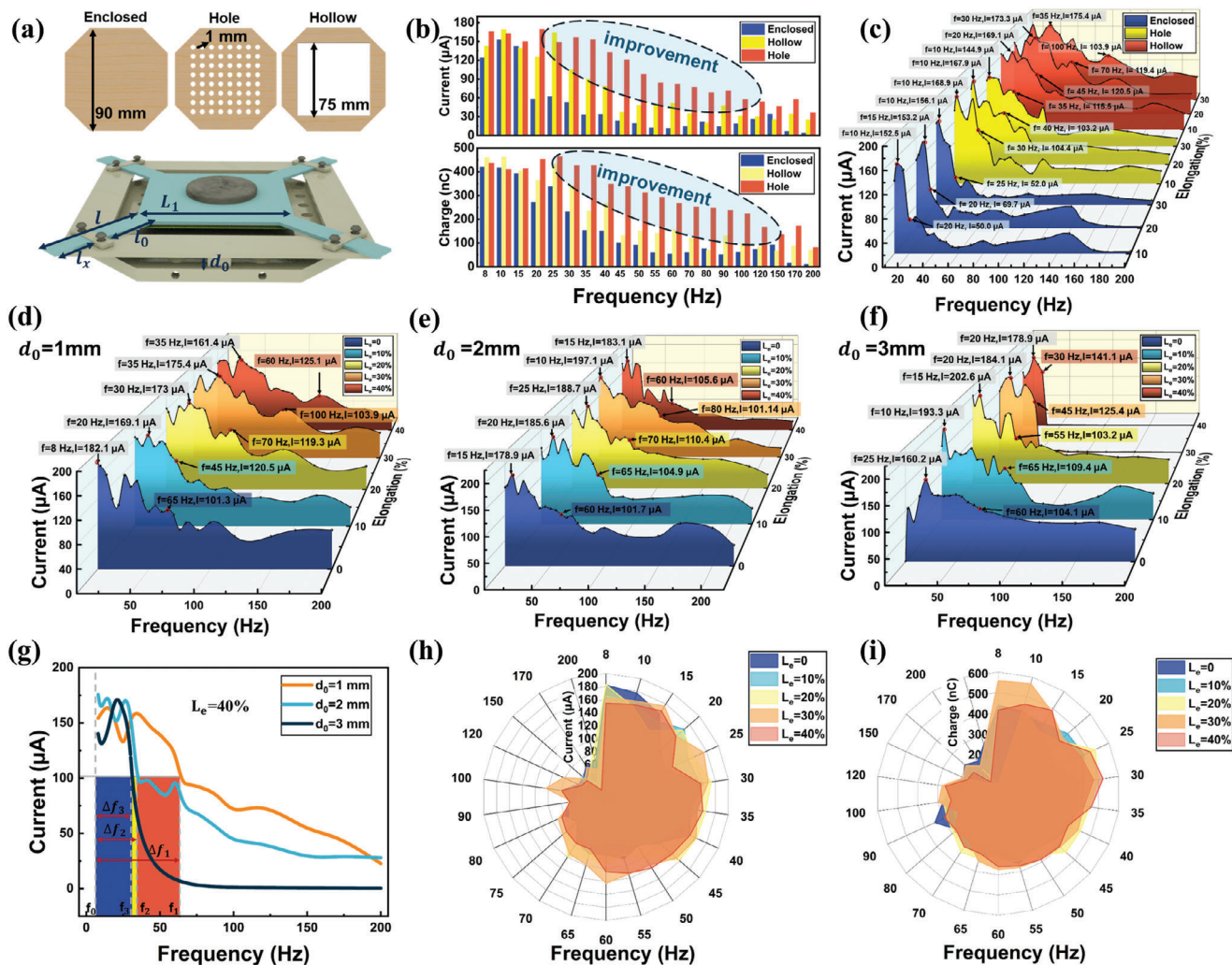
**ADVANCED
SCIENCE NEWS**

www.advancedsciencenews.com

**ADVANCED
ENERGY
MATERIALS**

www.advenergymat.de

Figure 4. Effect of the structural parameters on T-TVEH. a) Schematic diagram of various structural parameters of the T-TVEH and types of base plate including hollow, hole, and enclosed base plate. b) The I_{sc} and Q_{sc} of the T-TVEH dependent on the various base plates at the frequency of 8–200 Hz. c) The I_{sc} of the T-TVEH dependent on the permeability of base plate at the silicone elongation of 10%, 20%, and 30%. d–f) The I_{sc} the T-TVEH dependent on the various silicone elongation as the spacer size of 1, 2, and 3 mm. g) The I_{sc} of the T-TVEH dependent on the various spacer size at silicone elongation of 40%. The radargram of h) I_{sc} and i) Q_{sc} for the T-TVEH with different silicone elongation at spacer size of mm.

permeability (enclosed, hole, and hollow), are investigated. Figure 4b presents the I_{sc} and Q_{sC} of the T-TVEH with different base plates at frequency of 8–200 Hz. The results reveal that the EOP of the T-TVEH with different base plates exhibit relatively minor differences at frequency of 8–15 Hz. However, the EOP of the T-TVEH with a hole plate is noticeably higher than that with other types of plate when the frequency is greater than 15 Hz. For instance, the I_{sc} and Q_{sc} of the T-TVEH with enclosed and the hollow plate are 12.1 μA, 59.2 nC and 47.1 μA, 141.2 nC, respectively, at a frequency of 55 Hz. Whereas, they increase to 93.7 μA and 291.5 nC as the hole plate is utilized. The reason is that when the FEP film is tightly laminated to the conductive fabric, the air between them is drained, creating a confined space within the enclosed base plate. When the FEP film is forced to separate from the conductive fabric, the volume of the confined space increases, while the amount of air in the internal space remains unchanged. This generates internal and external pressure differ-

ences, thereby inhibiting the upward movement of the FEP film. However, due to the large amplitude and high input energy at low frequencies, the FEP film can overcome the pressure difference and contact with or separate from the conductive fabric. It is the opposite of the above results as the frequency increases. The influence of the pressure difference can be reduced by ameliorating the permeability of the base plate. Both hole and hollow plates exhibit excellent permeability. Nevertheless, the utilization of a hollow plate leads to insufficient contact between two dielectric materials, which reduces the charge transfer. Noteworthy is the fact that the base plate with evenly distributed holes not only demonstrates exceptional permeability but also ensures efficient contact between two dielectric materials. This characteristic significantly improves the EOP and working bandwidth of T-TVEH.

Considering that silicone elongation is an essential factor affecting the kinematic properties of T-TVEH. To comprehensively investigate the effect of base plate type on EOP, the I_{sc} and Q_{sc}

ADVANCED
SCIENCE NEWS

www.advancedsciencenews.com

ADVANCED
ENERGY
MATERIALS

www.advenergymat.de

of the T-TVEH with different base plates are individually measured at frequency of 8–200 Hz with various silicone elongations of 10%, 20%, and 30% (Figure 4c; Figure S4, Supporting Information). The experimental results exhibit that the T-TVEH with the hole plate always has excellent EOP regardless of the change in silicone elongation. The EOP and bandwidth of the T-TVEH with different silicone elongation are tested under the spacer size of 1, 2, and 3 mm, respectively. The overall trends for the I_{sc} of T-TVEH with different silicone elongation at spacer size of 1 mm can be seen in Figure 4d. The maximum I_{sc} of the T-TVEH reaches 182.1 µA with silicone elongation of 0, 12.8% higher than that with silicone elongation of 40%. In addition, Δf increased and then decreased with the increasing silicone elongation, reaching a maximum ($\Delta f = 92$ Hz) at silicone elongation is 30%. As shown in Figure 4e, the I_{sc} and Δf reach maximum ($I_{sc} = 197.1$ µA, $\Delta f = 72$ Hz) with silicone elongation of 30% and spacer size of 2 mm. When spacer size of 3 mm, the maximum values of the I_{sc} and Δf for the T-TVEH are 202.6 µA and 50 Hz, respectively (Figure 4f). Similar results can also be found for the Q_{sc} of the T-TVEH (Figure S5, Supporting Information). Therefore, the maximum I_{sc} of the T-TVEH increases slightly with increasing spacer size, but the maximum Δf is significantly reduced. This is because the increase of the spacer size enhances the maximum relative displacement between two dielectric materials but reduces the contact force at the high-frequency band range.

To further evaluate the effect of spacer size on the bandwidth of the T-TVEH, the EOP of the T-TVEH with different spacer size and the same silicone elongation are compared separately. As shown in Figure 4g, there is no significant difference in the I_{sc} when the frequency is lower than 30 Hz. The I_{sc} is significantly higher when frequencies exceed 30 Hz with a spacer size of 1 mm compared to the other two conditions. Comparison results at other silicone elongation can be found in Figure S6 (Supporting Information). Obviously, the bandwidth of the T-TVEH is widest and exhibits excellent EOP as spacer size is 1 mm. To comprehensively analyze the influence of silicone elongation on the EOP of the T-TVEH, the I_{sc} and Q_{sc} with different silicone elongation under spacer size is 1 mm (at the frequency range of 8 to 200 Hz) are shown in Figure 4h,i. It is found that the optimal silicone elongation, maximizing the EOP of the T-TVEH, varies under different frequencies. Specifically, when the frequency is below 20 Hz, the optimal EOP of the T-TVEH achieves at smaller silicone elongation. However, if the frequency is above 20 Hz, the optimal EOP of the T-TVEH achieves at silicone elongation is 30%. Therefore, the optimal elongation is finally determined as silicone elongation is 30%.

2.5. Performance of the T-TVEH

The diversity of mechanical devices and the randomness of vibrations lead to a wide range of frequencies and accelerations for vibration excitation in real scenarios. Therefore, it is crucial to further analyze the effect of different accelerations on the EOP of T-TVEH in a wide bandwidth range. **Figure 5a**, S7 (Supporting Information) show the Q_{sc} and I_{sc} of the T-TVEH under acceleration ranging from 10 to 40 m s^{-2} within the frequency range of 8 to 200 Hz. The experimental results illustrate a positive correlation between the vibration acceleration and the enhancement

of EOP. The T-TVEH demonstrates excellent acceleration adaptability, which is capable of generating maximum EOP of 42.7 µA, and 30 nC at the acceleration of only 10 m s^{-2}. At the same time, the maximum EOP increases to 172 µA and 482.6 nC under the acceleration of 40 m s^{-2}. Besides the effect on energy harvesting, the frequency itself is also a vital parameter to reflect the operational status of mechanical equipment, which can be analyzed with the Fast Fourier Transform (FFT). Figure 5b compares the frequency after FFT analysis of the current signal with the actual frequency of the vibration excitation. Meanwhile, the frequency after FFT processing under the frequency is 8–250 Hz is shown in Figure S8 (Supporting Information). The result reveals that the error is negligible compared to the actual value ($R^2 = 0.9998$), which proves the capability of the T-TVEH as a self-powered frequency sensor. As shown in Figure S9 (Supporting Information), the durability of T-TVEH is fully evaluated under a frequency of 100 Hz and acceleration of 30 ms^{-2}. After up to 19000 cycles, the output current of the T-TVEH remains (basically) unchanged (Figure S9a, Supporting Information). As shown in Figure S9b (Supporting Information), the surface quality of FEP film and conductive fabric by SEM before/after the operation for 19000 cycles are compared. Test results show barely changes in the surface quality of FEP film and conductive fabric after the operation for 19000 cycles, which reflecting the excellent durability of the T-TVEH.

The power density and capacitor charging capability are critical indicators for evaluating T-TVEH as a power source. The maximum output power is obtained by matching different impedance, which is illustrated in Figure 5c. The I_{sc} of the T-TVEH decreases with the increase of load resistance. The maximum power density reaches 5.9 W m^{-2} at the load resistance of 4 MΩ. In addition, due to the ultra-wide bandwidth of the T-TVEH, the peak power of the T-TVEH is measured under frequencies from 8 to 220 Hz. Subsequently, the average power $P_{Average}$ is calculated. This can be expressed as:

$$P_{Average} = \frac{\int_0^T I_{sc}{}^2 R dt}{T} \tag{8}$$

where T is the period of vibration excitation, R is the load resistance value. As shown in Figure 5d, although the power of the T-TVEH decreases nonlinearly with increasing frequency, the peak power is maintained at 3.2 mW under the frequency of 200 Hz. Furthermore, the magnitude of the average power is correlated with both the frequency and the EOP of the T-TVEH. It exhibits an initial increase followed by a subsequent decrease with rising frequency and reaches its maximum at a frequency of 100 Hz ($P_{Average} = 3.85$ mW).

Furthermore, the capacitance charging capability of the T-TVEH is tested from 15 to 200 Hz with a capacitance of 1000 µF under the acceleration of 30 m s^{-2}. As shown in Figure 5e, the charging performance of the T-TVEH increases with frequency and reaches its maximum at 100 Hz. Specifically, a 1000 µF capacitor could be charged to 3 V within 70 s, which proves the excellent capacitive charging capability of T-TVEH. However, the charging performance of the T-TVEH is not only affected by the EOP but also by the frequency. To explore the factors affecting the charging performance of the T-TVEH, the average power and capacitor charging time (voltage from 0 to 3 V) of the T-TVEH
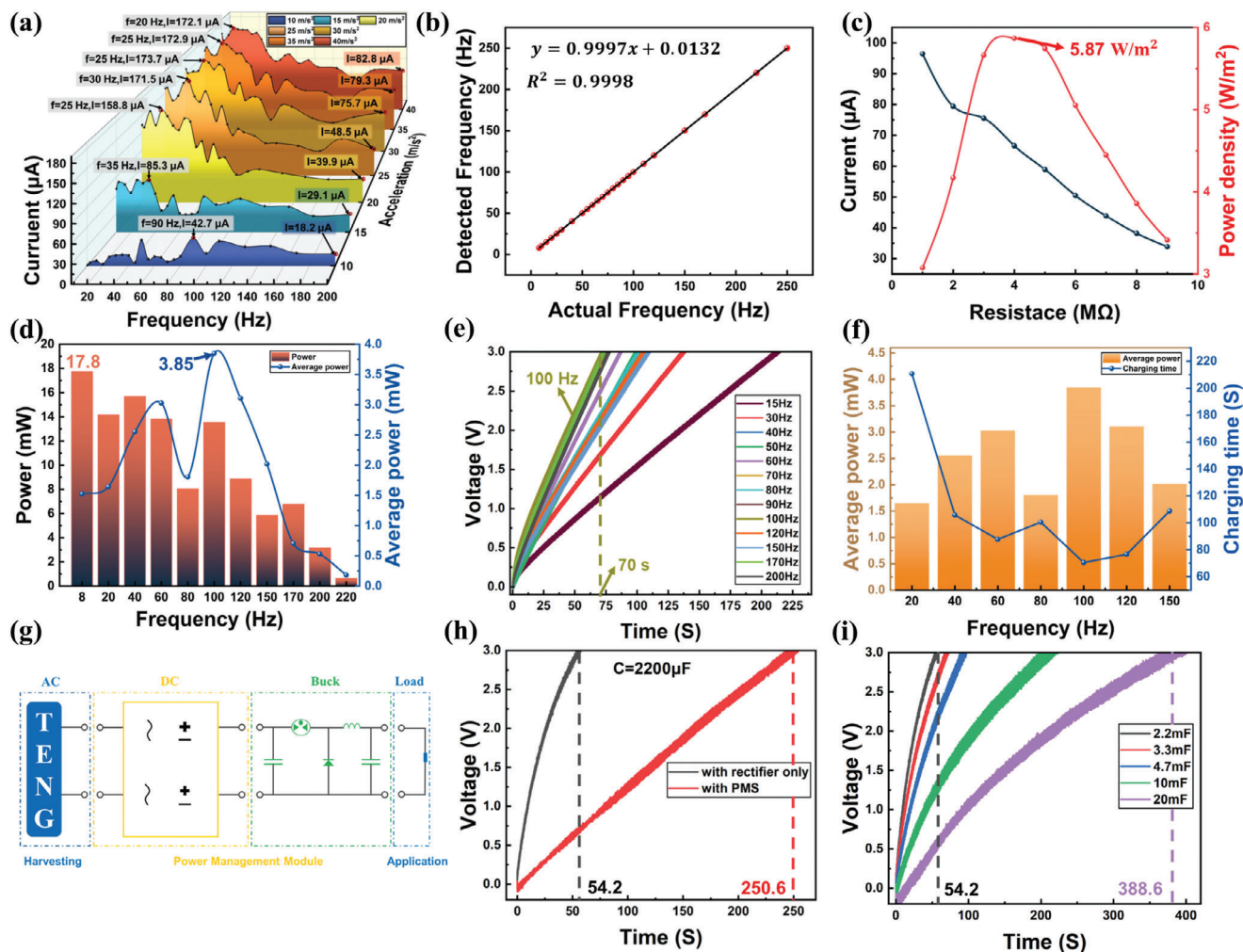
**ADVANCED
SCIENCE NEWS**

www.advancedsciencenews.com

**ADVANCED
ENERGY
MATERIALS**

www.advenergymat.de

Figure 5. The EOP and charging performance of the T-TVEH. a) Effect of acceleration on the I_{sc} of the T-TVEH at frequency of 8–200 Hz. b) The relationship between the exciting frequency and detected frequency of I_{sc} at frequency of 8–250 Hz. c) The I_{sc} and power density depend on the load resistance. d) The peak power and average power of the T-TVEH at the frequency of 8–220 Hz and $a_m = 30$ m s^{-2}. e) Charging performance of the T-TVEH at the frequency of 15–200 Hz. f) Charging performance of the T-TVEH at the frequency of 15–200 Hz. g) Schematic of the current of the PMS. h) Comparison of T-TVEH with PMS and T-TVEH with rectifier for supercapacitor charging efficiency. i) Charging efficiency of the T-TVEH when the capacitance value of supercapacitor from 2.2 to 20 mF.

at different frequencies are studied, which is demonstrated in Figure 5f. It reveals that the capacitor charging performance is positively correlated with the average power of T-TVEH. This further underlines the excellent frequency adaptability of the T-TVEH.

Nevertheless, the wireless sensing systems require high-capacity supercapacitors to power. Although the T-TVEH provides a relatively high output current, the inherent characteristic of the T-TVEH limits its charging performance for supercapacitors. The Power Management System (PMS) is used to improve the charging performance of the T-TVEH significantly. Figure 5g illustrates the circuit diagram of the PMS. Compared to the capacitor charging performance of the T-TVEH only with a rectifier, it is significantly improved after applying the PMS, the comparison between them is exhibited in Figure 5h. It takes 250.6 s to charge a 2200 µF capacitor from 0 to 3 V at a frequency of 100 Hz by the T-TVEH only with rectifier, but it only requires 54.2 s

by the T-TVEH with PMS. The charging performance is notably enhanced through the integration of the PMS. As shown in the Figure 5i, even a 20 mF supercapacitor could be charged to 3 V within 388.6 s, laying a crucial foundation for establishing totally self-powered wireless sensing systems in the subsequent stages.

2.6. Application Demonstration of the T-TVEH

Based on the excellent electrical output and sensing performance of T-TVEH, the fully self-powered wireless sensor node for monitoring machinery conditions with characteristics such as low power consumption, long-distance, and high adaptability is constructed. The wireless sensor node comprises four key components, including wireless sensor, MCU, wireless communication module, and terminal display module (**Figure 6a**). In addition, the output of multiple T-TVEHs are effectively integrated by
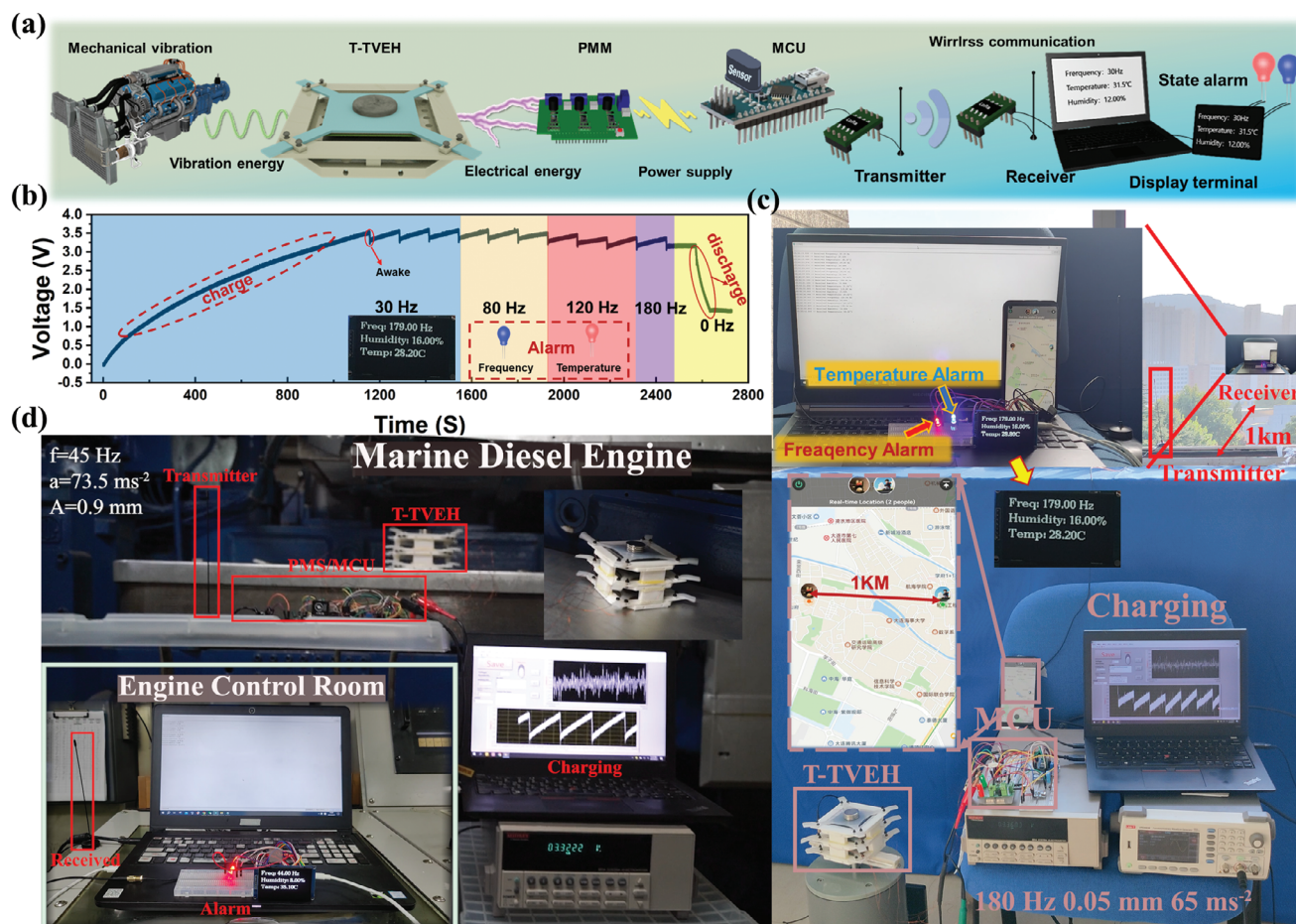
Figure 6. Application Demonstrations of the T-TVEH. a) The workflow diagram of wireless sensor node. b) The voltage variations throughout the process of the supercapacitor at the T-TVEH supplying energy to the wireless sensor node. The wireless sensor node was working on c) the shaker and d) real ship diesel engines.

stacking, significantly improving the charging efficiency of 0.1 F supercapacitors, ensuring sufficient power for the entire system. The corresponding circuit diagram is shown in Figure S10 (Supporting Information). This provides innovative insights and performance optimization for the practical application of vibration energy harvesting technology. The vibration frequency of the mechanical equipment, the surrounding temperature, and humidity are determined to be captured due to their significance to assess the working condition of the equipment. The LoRa-based wireless communication module is used for long-distance wireless transmission of information. The sensors and LoRa module are integrated into the MCU, enabling efficient data collection and remote communication. Finally, the sensing data is showcased on the computers and OLED screens, with different colored LEDs indicating abnormal states.

Initially, the performance of wireless sensor node is comprehensively tested using a shaker to simulate mechanical vibrations. The voltage variations of the 0.1 F supercapacitor throughout the whole powering and signal transmitting process are represented in Figure 6b. The voltage of the supercapacitor reaches 3.5 V within 1154 s, and then after the powering process starts, the initial information acquisition and wireless transmission

consumes a large amount of energy. This causes the voltage of the supercapacitor to drop rapidly. Subsequently, after the first data transfer is completed, the MCU goes to sleep controlled by the timer with the monitoring period set to 2 min. At this time, the MCU is in a low-power consumption state, and the power of the supercapacitor is continuously replenished by the T-TVEH for the subsequent normal operation. To assess the performance of wireless sensor node across a broad bandwidth of vibration excitations, experiments are conducted under frequency of 30, 80, 120, and 180 Hz, respectively. The test results reveal that the wireless sensor node operates reliably and consistently irrespective of variations in frequency. This demonstrates the robustness and its capability of wireless sensor node to function effectively across a diverse range of mechanical vibration frequencies.

Even more, the T-TVEH's excellent capacitive charging capability enables the wireless sensor node to transmit information wirelessly over long-distances. In order to evaluate the performance of the system for long-distance state detection, the transmitter and receiver of LoRa are placed at a test field 1000-m away from each other. The complete process of the test at frequencies of 30, 120, and 180 Hz are recorded as shown in Figure 6c and Movie S2 (Supporting Information). Among, the test conditions

include: frequency of 30 Hz, amplitude of 0.83 mm and acceleration of 30 m s^{-2}; frequency of 120 Hz, amplitude of 0.09 mm and acceleration of 53 m s^{-2}; frequency of 180 Hz and, amplitude of 0.05 mm and acceleration of 65 m s^{-2}, respectively. The temperature, humidity, and frequency information were successfully acquired and transmitted to 1000-m through the wireless sensor node, which is a 9 times improvement compared to related studies. Simultaneously, the machinery condition is conveyed through the illumination and extinguishing of LEDs. Specifically, an abnormal condition is indicated by setting the temperature exceeding 30 °C and the frequency over 120 Hz. In this scenario, the red LED lights up to signify an abnormal temperature, while the blue LED lights up to indicate an abnormal frequency state. This excellent result demonstrates the feasibility of employing the T-TVEH for totally self-powered long-distance wireless machinery condition monitoring. As shown in Figure S11 (Supporting Information), the ranges of vibration frequency, amplitude and acceleration that can minimally maintain the self-powered operation of the constructed system is further explored. The minimum acceleration to charge a 0.1 F supercapacitor to 3.5 V at 8–200 Hz is evaluated. The experimental results show that the system can be operated in the frequency range of 8–200 Hz, in which the minimum acceleration required to maintain normal operation of the system is 12 m s^{-2}, and minimum amplitude is 0.04 mm.

However, the operational conditions of machinery and equipment are often characterized by instability, particularly in environments with high temperatures and dust. This is especially true for machinery and equipment within the ship engine room, where exists a significant amount of unutilized vibration energy, as well as high decibels of noise and heat. This wireless sensor node provides a novel approach for monitoring the operational status of machinery wirelessly. To test the performance of the wireless sensor node in actual scenarios, the T-TVEH is arranged on the marine diesel generator of an actual teaching vessel named YU KUN as shown in Figure 6d. The V_{oc}, I_{sc}, and Q_{sc} of a single T-TVEH in actual teaching vessel is tested (Figure S12, Supporting Information). The results show that the V_{oc}, I_{sc}, and Q_{sc} of the T-TVEH are 324.1 V, 138 μA, and 357 nC, respectively. Meanwhile, using three T-TVEH together to charge a 0.1 F supercapacitor, which is charged from 0 to 3 V in 567 s (Figure S13, Supporting Information). This demonstrates the high applicability of T-TVEH and its effectiveness in providing in- situ energy supply for the wireless sensor node. The transmitter of the LoRa is placed near the T-TVEH, and the receiver, the terminal display, and the alarm device are placed in the engine control room (ECR). The voltage variations of supercapacitor throughout the process for wireless sensor node working is shown in Figure S14 (Supporting Information). Ultimately, the wireless sensor node transmits the collected vibration frequency of the diesel engine, surrounding temperature and humidity information to the ECR with terminal display and abnormal alarms (Movie S3, Supporting Information). The application in a real ship diesel engine demonstrated its feasibility in practical uses.

3. Conclusion

In summary, a high performance and stackable trampoline like-triboelectric vibration energy harvester (T-TVEH) was de-veloped to efficiently harvest ultra-wideband vibrational energy and then provide in-situ energy supply to the sensor nodes. The structural parameters of T-TVEH were optimized by theoretical and experimental analyses. The results show that the unique structural design and material selection enable T-TVEH to generate excellent electrical output performance over an ultra-wideband of 8–200 Hz. Remarkably, even at an extremely high frequency (200 Hz) and low amplitude (0.019 mm), the T-TVEH maintains exceptional output of 79.3 μA and 238.6 nC. Therefore, the T-TVEH represents a breakthrough in terms of both working bandwidth and power density compared to recent research efforts in the field of vibration energy harvesting. Specifically, the working bandwidth of T-TVEH is 156% higher than in previous studies. The peak power density of T-TVEH reaches 5.9 W m^{-2}, which is a 59.2% increase compared to the best results from recent related research work. It maintains stable electrical output performance and material surface quality after up to 19000 cycles, which reflecting the excellent durability of the T-TVEH. The power management strategy is designed to enhance the capacitor charging efficiency of the T-TVEH. In addition, the capacitor charging performance is found to be positively correlated with the average power. Based on the excellent performance of TVEH a fully self-powered wireless sensor node for monitoring machinery condition is constructed. The temperature, humidity and vibration frequency are successfully captured and transmitted to 1000-m through the wireless sensor node, which is a 9 times improvement compared to the best results from the related studies. Finally, it achieves totally self-powered wireless operation monitoring and abnormal alarm on a marine diesel engine of real ship. The results in this work show that the T-TVEH has great potential applications for accomplishing in-situ self-powered WSNs in the era of IoT.

4. Experimental Section

Fabrication of the T-TVEH: The T-TVEH consists of conductive fabric, silicone, FEP film with conductive ink printed on one side adhered to an iron plate, additional mass, conductive sponge, separation layer, base plate with evenly distributed holes, and silicone tensioning device. The additional mass was made of metal and the weight is adjusted by changing the volume. The size of conductive fabric, conductive sponge, and FEP film were 5.5 × 5.5 cm, with thicknesses of 100 μm, 1 mm, and 50 μm, respectively. The spacer with thickness of 1, 2, 3 mm, base plate with holes' diameter of 1 mm, and silicone tensioning device were produced by 3D printing. The Ecoflex 0030 Parts A and B were utilized to fabricate the silicone (thickness of 2 mm) with mixing ratio of 1:1. The four corners (initial length of 40 mm) of the silicone were fixed by the silicone tensioning device, which was adjusted by the elongation through the control of l_x length. The FEP flim was adhered to an iron plate to ensure that it without deformation in motion and thus has a good contact effect with the conductive fabric.

Motion Observation and Electrical Measurements of the T-TVEH: The high-speed camera (PHANTOM @24VDC) was applied to observe the motion of the T-TVEH in a shaker. The amplitude sensor (HG-C1100) was used to measure the amplitude of the FEP film. The shaker (JZK-50) was employed to simulate mechanical vibration, the amplitude and frequency of which was controlled by a signal generator (UTG2062B) with the signal amplified by a power amplifier (YE5874A). The vibration acceleration of T-TVEH in a shaker was measured by an acceleration sensor (KS 96.100) together with a signal processing unit (YND-1504). The electric output signals (V_{oc}, I_{sc}, and Q_{sc}) were measured by an electrometer (Keithley 6514).

Supporting Information

Acknowledgements

Conflict of Interest

The authors declare no conflict of interest.

Data Availability Statement

The data that support the findings of this study are available from the corresponding author upon reasonable request.

Keywords

[1] W. Z. Khan, M. H. Rehman, H. M. Zangoti, M. K. Afzal, N. Armi, K. Salah, *Comput. Electr. Eng.* **2020**, *81*, 106522.

[2] E. Sisinni, A. Saifullah, S. Han, U. Jennehag, M. Gidlund, *IEEE Trans. Ind. Informat.* **2018**, *14*, 4724.

[3] M. Abdulkarem, K. Samsudin, F. Z. Rokhani, M. F. A. Rasid, *Struct. Health Monit.* **2020**, *19*, 693.

[4] T. L. Du, F. Y. Dong, Z. Y. Xi, M. X. Zhu, Y. J. Zou, P. T. Sun, M. Y. Xu, *Small* **2023**, *19*, 2300401.

[5] V. J. Hodge, S. O'Keefe, M. Weeks, A. Moulds, *IEEE Trans. Intell. Transp. Syst.* **2015**, *16*, 1088.

[6] I. El-Thalji, E. Jantunen, *Mech. Syst. Signal Process* **2015**, *252*, 60.

[7] T. Han, C. Liu, W. G. Yang, D. X. Jiang, *Knowledge Based Syst.* **2019**, *165*, 474.

[8] X. Zhao, H. Askari, J. Chen, *Joule* **2021**, *5*, 1391.

[9] B. Rashid, M. H. Rehmani, *J. Network Comput. Appl.* **2016**, *60*, 192.

[10] H. Wu, J. Y. Wang, Z. Y. Wu, S. L. Kang, X. L. Wei, H. Q. Wang, H. Luo, L. J. Yang, R. J. Liao, Z. L. Wang, *Adv. Energy Mater.* **2022**, *12*, 2103654.

[11] C. Zhao, Z. Y. Wang, Y. W. Wang, Z. Qian, Z. Tan, Q. Y. Chen, X. X. Pan, M. Y. Xu, Y. C. Lai, *Adv. Funct. Mater.* **2023**, *33*, 2306381.

[12] R. Y. Liu, Z. L. Wang, K. Fukuda, T. Someya, *Nat. Rev. Mater.* **2022**, *7*, 870.

[13] T. Rault, A. Bouabdallah, Y. Challal, *Comput. Networks* **2014**, *67*, 104.

[14] C. Q. Zhu, M. W. Wu, C. Liu, C. Xiang, R. J. Xu, H. Y. Yang, Z. Y. Wang, Z. Y. Wang, P. Xu, F. Z. Xing, H. Wang, M. Y. Xu, *Adv. Energy Mater.* **2023**, *13*, 2301665.

[15] J. J. Luo, W. C. Gao, Z. L. Wang, *Adv. Mater.* **2021**, *33*, 2004178.

[16] P. Huang, L. Xiao, S. Soltani, M. W. Mutka, N. Xi, *IEEE Commun. Surveys Tuts.* **2013**, *15*, 101.

[17] L. Liu, X. G. Guo, C. Lee, *Nano Energy* **2021**, *88*, 106304.

[18] J. Yang, J. Chen, Y. Yang, H. L. Zhang, W. Q. Yang, P. Bai, Y. J. Su, Z. L. Wang, *Adv. Energy Mater.* **2014**, *4*, 1301322.

[19] H. F. Zhao, X. Xiao, P. Xu, T. C. Zhao, L. G. Song, X. X. Pan, J. C. Mi, M. Y. Xu, Z. L. Wang, *Adv. Energy Mater.* **2019**, *9*, 1902824.

[20] C. F. Wei, X. J. Jing, *Renew Sustain. Energy Rev.* **2017**, *74*, 1.

[21] M. Y. Xu, P. H. Wang, Y. C. Wang, S. L. Zhang, A. C. Wang, C. L. Zhang, Z. J. Wang, X. X. Pan, Z. L. Wang, *Adv. Energy Mater.* **2018**, *8*, 1702432.

[22] L. C. Zhao, H. X. Zou, K. X. Wei, S. X. Zhou, G. Meng, W. M. Zhang, *Adv. Energy Mater.* **2023**, *13*, 2300557.

[23] G. Zhu, B. Peng, J. Chen, Q. S. Jing, Z. L. Wang, *Nano Energy* **2015**, *14*, 126.

[24] M. Willatzen, Z. L. Wang, *Nano Energy* **2018**, *52*, 517.

[25] S. M. Niu, S. H. Wang, L. Lin, Y. Liu, Y. S. Zhou, Y. F. Hu, Z. L. Wang, *Energy Environ. Sci.* **2013**, *6*, 3576.

[26] T. C. Zhao, M. Y. Xu, X. Xiao, Y. Ma, Z. Li, Z. L. Wang, *Nano Energy* **2021**, *88*, 106199.

[27] H. F. Zhao, M. Y. Xu, M. R. Shu, J. An, W. B. Ding, X. Y. Liu, S. Y. Wang, C. Zhao, H. Y. Yu, H. Wang, C. Wang, X. P. Fu, X. X. Pan, G. M. Xie, Z. L. Wang, *Nat. Commun.* **2022**, *13*, 3325.

[28] K. Dong, X. Peng, R. W. Cheng, C. A. Ning, Y. Jiang, Y. H. Zhang, Z. L. Wang, *Adv. Mater.* **2022**, *34*, 2109355.

[29] Y. C. Qi, G. X. Liu, Y. Y. Gao, T. Z. Bu, X. H. Zhang, C. Q. Xu, Y. Lin, C. Zhang, *ACS Appl. Mater. Interfaces* **2021**, *13*, 26084.

[30] T. Quan, Y. C. Wu, Y. Yang, *Nano Res.* **2015**, *8*, 3272.

[31] X. Xiao, X. Q. Zhang, S. Y. Wang, H. Ouyang, P. F. Chen, L. G. Song, H. C. Yuan, Y. L. Ji, P. H. Wang, Z. Li, M. Y. Xu, Z. L. Wang, *Adv. Energy Mater.* **2019**, *9*, 1902460.

[32] X. F. Wang, S. M. Niu, F. Yi, Y. J. Yin, C. L. Hao, K. Dai, Y. Zhang, Z. You, Z. L. Wang, *ACS Nano* **2017**, *11*, 1728.

[33] C. Wu, J. H. Park, B. Koo, X. Y. Chen, Z. L. Wang, T. W. Kim, *ACS Nano* **2018**, *12*, 9947.

[34] Y. C. Qi, G. X. Liu, Y. Kuang, L. Wang, J. H. Zeng, Y. Lin, H. Zhou, M. L. Zhu, C. Zhang, *Nano Energy* **2022**, *99*, 107427.

[35] T. L. Du, D. L. Shen, Z. Y. Xi, H. Y. Yu, F. Y. Dong, C. Zhao, M. X. Zhu, Y. J. Zou, P. T. Sun, M. Y. Xu, *Nano Res.* **2023**.

[36] Y. Wang, Y. S. Wu, Q. Liu, X. D. Wang, J. Cao, G. G. Cheng, Z. Q. Zhang, J. M. Ding, K. Li, *Energy* **2020**, *212*, 118462.

[37] H. Wu, Z. H. Wang, B. Y. Zhu, H. Q. Wang, C. Y. Lu, M. C. Kang, S. L. Kang, W. B. Ding, L. J. Yang, R. J. Liao, J. Y. Wang, Z. L. Wang, *Adv. Energy Mater.* **2023**, *13*, 2300051.

[38] N. Tran, M. H. Ghayesh, M. Arjomandi, *Int. J. Eng. Sci.* **2018**, *127*, 162.

[39] D. Guan, G. Q. Xu, X. Xia, J. Q. Wang, Y. L. Zi, *ACS Appl. Mater. Interfaces* **2021**, *13*, 6331.

[40] Z. W. Ren, L. T. Wu, J. J. Zhang, Y. Wang, Y. Wang, Q. K. Li, F. Wang, X. Liang, R. S. Yang, *ACS Appl. Mater. Interfaces* **2022**, *14*, 5497.

[41] Y. C. Qi, Y. Kuang, Y. Y. Liu, G. X. Liu, J. H. Zeng, J. Q. Zhao, L. Wang, M. L. Zhu, C. Zhang, *Appl. Energy* **2022**, *327*, 120092.

[42] X. S. Zhang, Y. Yu, X. Xia, W. Q. Zhang, X. J. Cheng, H. Y. Li, Z. L. Wang, T. H. Cheng, *Adv. Energy Mater.* **2023**, *13*, 2302353.

[43] L. Zhang, L. Jin, B. B. Zhang, W. L. Deng, H. Pan, J. F. Tang, M. H. Zhu, W. Q. Yang, *Nano Energy* **2015**, *16*, 516.

[44] J. Chen, G. Zhu, W. Q. Yang, Q. S. Jing, P. Bai, Y. Yang, T. C. Hou, Z. L. Wang, *Adv. Mater.* **2013**, *25*, 6094.

[45] D. Bhatia, W. Kim, S. Lee, S. W. Kim, D. Choi, *Nano Energy* **2017**, *33*, 515.

[46] C. C. Yang, G. L. Liu, X. J. Wang, B. X. Liu, L. F. Xiao, L. Y. Wan, H. L. Yao, *Adv. Mater. Technol.* **2023**, *8*, 2200465.

[47] Y. Song, J. H. Min, Y. Yu, H. B. Wang, Y. R. Yang, H. X. Zhang, W. Gao, *Sci. Adv.* **2020**, *6*, 9842.

ADVANCED
SCIENCE NEWS

www.advancedsciencenews.com

ADVANCED
ENERGY
MATERIALS

www.advenergymat.de

[48] L. Wang, T. Y. Y. He, Z. X. Zhang, L. B. Zhao, C. K. Lee, G. X. Luo, Q. Mao, P. Yang, Q. J. Lin, X. Li, R. Maeda, Z. D. Jiang, *Nano Energy* **2021**, *80*, 105555.

[49] Y. L. Chen, D. Liu, S. Wang, Y. F. Li, X. S. Zhang, *Nano Energy* **2019**, *64*, 103911.

[50] S. S. K. Mallineni, Y. C. Dong, H. Behlow, A. M. Rao, R. Podila, *Adv. Energy Mater.* **2018**, *8*, 1702736.

[51] H. Y. Wang, J. Q. Wang, K. M. Yao, J. J. Fu, X. Xia, R. R. Zhang, J. Y. Li, G. Q. Xu, L. Y. Wang, J. C. Yang, J. Lai, Y. Dai, Z. Y. Zhang, A. Y. Li, Y. Y. Zhu, X. G. Yu, Z. L. Wang, Y. L. Zi, *Sci. Adv.* **2021**, *7*, eabi6751.

[52] Z. H. Wang, Y. C. Jin, C. Y. Lu, J. Y. Wang, Z. W. Song, X. Yang, Y. D. Cao, Y. L. Zi, Z. L. Wang, W. B. Ding, *Energy Environ. Sci.* **2022**, *15*, 2983.

[53] Z. Wang, G. X. Liu, J. Cao, X. P. Fu, B. B. Fan, Y. H. Qin, Z. Z. Wang, Z. Zhang, Y. F. Chen, C. Zhang, *Adv. Mater. Technol.* **2023**, *8*, 23004.

[54] S. M. Niu, Z. L. Wang, *Nano Energy* **2015**, *14*, 161.

[55] W. G. Kim, D. W. Kim, I. W. Tcho, J. K. Kim, M. S. Kim, Y. K. Choi, *ACS Nano* **2021**, *15*, 258.

[56] T. Zhou, C. Zhang, C. B. Han, F. R. Fan, W. Tang, Z. L. Wang, *ACS Appl. Mater. Interfaces* **2014**, *6*, 14695.